Magma intrusion and volatile ascent beneath Norris Geyser Basin, Yellowstone National Park

Charles Wicks[1], Daniel Dzurisin[2], Jacob Lowenstern[2], and Jerry Svarc[1]

[1]U.S. Geological Survey
[2]USGS

November 22, 2022

Abstract

Recent activity has provided new insights into the causes of surface deformation in and around the Yellowstone Caldera, a topic that has been debated since the discovery of caldera-floor uplift more than four decades ago. An episode of unusually rapid uplift (>15 cm/yr) centered near Norris Geyser Basin along the north caldera rim began in late 2013 and continued until a Mw 4.9 earthquake on 30 March 2014; thereafter, uplift abruptly switched to subsidence. Uplift at rates of several cm/yr resumed in 2016 and continued at least through the end of 2018. Modeling of Global Positioning System (GPS) and interferometric synthetic aperture radar (InSAR) data suggests an evolving process of deep magma intrusion during 1996-2001 followed by volatile ascent and accumulation at shallow levels, perhaps as shallow as a few hundred meters depth. The preferred deformation model in which the volatiles accumulated is a shallow uplifted (domed) reservoir. The depth of shallow volatile accumulation appears to have shallowed from the 2014 to the 2016 deformation episode, from 3.2 km depth to 1.8 km depth respectively, and frequent eruptions of Steamboat Geyser since March 2018 might be a surface manifestation of this ongoing process. Hydrothermal explosion features are prominent in the Norris Geyser Basin area, and the apparent shallow nature of the inferred volatile accumulation might represent an increased risk of hydrothermal explosions in the vicinity of Norris Geyser Basin.

V33D-0198

Magma intrusion and volatile ascent beneath Norris Geyser Basin, Yellowstone National Park

Charles Wicks, Dan Dzurisin, Jacob Lowenstern, and Jerry Svarc

Summary

An episode (the 2014 episode) of unusually rapid uplift (>15 cm/yr) centered near Norris Geyser Basin (NGB) along the north caldera rim began in late 2013 and continued until a Mw 4.9 earthquake on 30 March 2014; thereafter, uplift abruptly switched to subsidence. Uplift at rates of several cm/yr resumed in 2016 and continued at least through the end of 2018 (the 2016 episode). Modeling of Global Positioning System (GPS) and interferometric synthetic aperture radar (InSAR) data suggests an evolving process of deep magma intrusion during 1996-2001 (the 2000 episode) followed by volatile ascent and accumulation at shallow levels, perhaps as shallow as a few hundred meters depth. The depth of shallow volatile accumulation appears to have further shallowed from the 2014 to the 2016 deformation episode and frequent eruptions of Steamboat Geyser since March 2018 are likely a surface manifestation of this ongoing process. Hydrothermal explosion features are prominent in the Norris Geyser Basin area, and the uplift and apparent shallow nature of the volatile accumulation implies an increased risk of hydrothermal explosions.

I. Setting

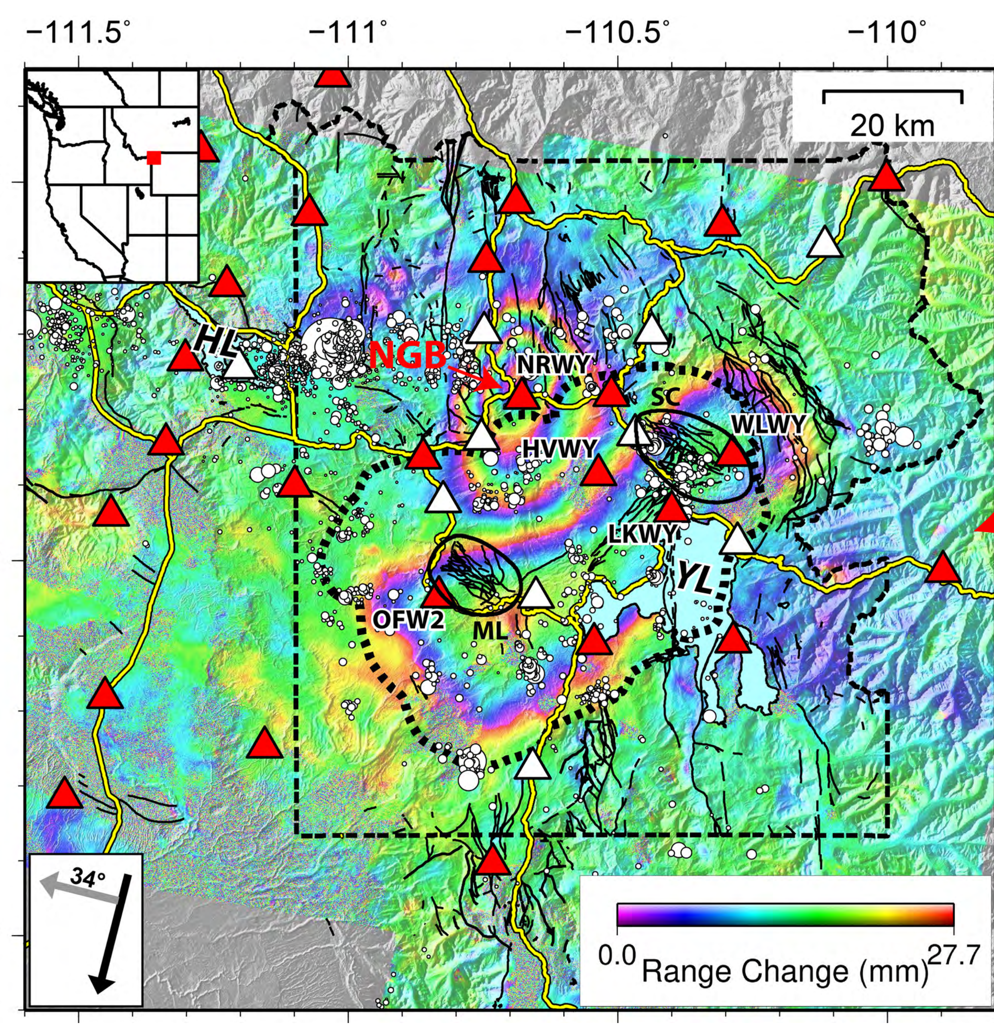

Deformation in Yellowstone is known mostly for the caldera uplift/subsidence cycles. The Sentinel 1 interferogram in Figure 1 shows caldera subsidence, but it also shows simultaneous uplift beneath Norris Geyser Basin, an area of high heat flow and plentiful thermal features, just outside of the north caldera rim. Three distinct episodes of deformation have been recorded in the area of the north caldera rim.

Figure 1 -- Information map for Yellowstone. The location of Yellowstone is shown with the red square in the regional inset map of the western United States. The Sentinel 1 interferogram shown spans 20150609 to 20170704. Plotted earthquakes are from the U. of Utah Seismographic Stations catalog.

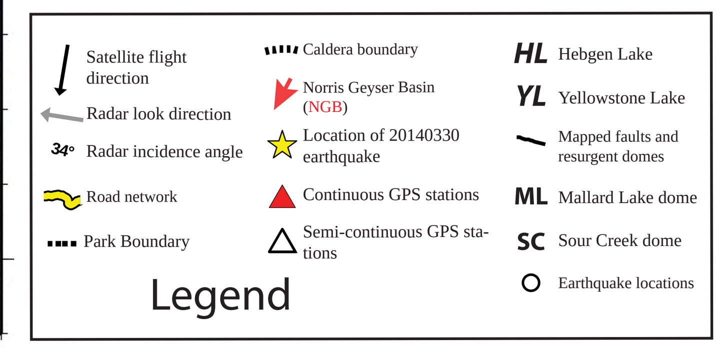

II. Three North Rim Deformation Episodes

The vertical GPS record from continuous GPS station NRWY, nearest to Norris Geyser Basin, in Fig. 2 shows the time evolution of the three north rim deformation episodes. The three descending interferograms in Fig. 3 (and GPS offset vectors in Fig. 3b) show the areal signature of the three episodes of deformation. Note the change in size of the area of measured deformation in each interferogram, and the change in position of the center of deformation. The data set for the 2014 episode consists of seven interferograms (six from TerraSAR-X, and one from RADARSAT-2) and three discrete surface displacement measurements from continuous and semi-continuous GPS stations. The data set for the 2016 episode consists of six interferograms (one TerraSAR-X, one ALOS2, and four Sentinel 1) and one set of discrete displacement measurements from continuous and semi-continuous GPS stations.

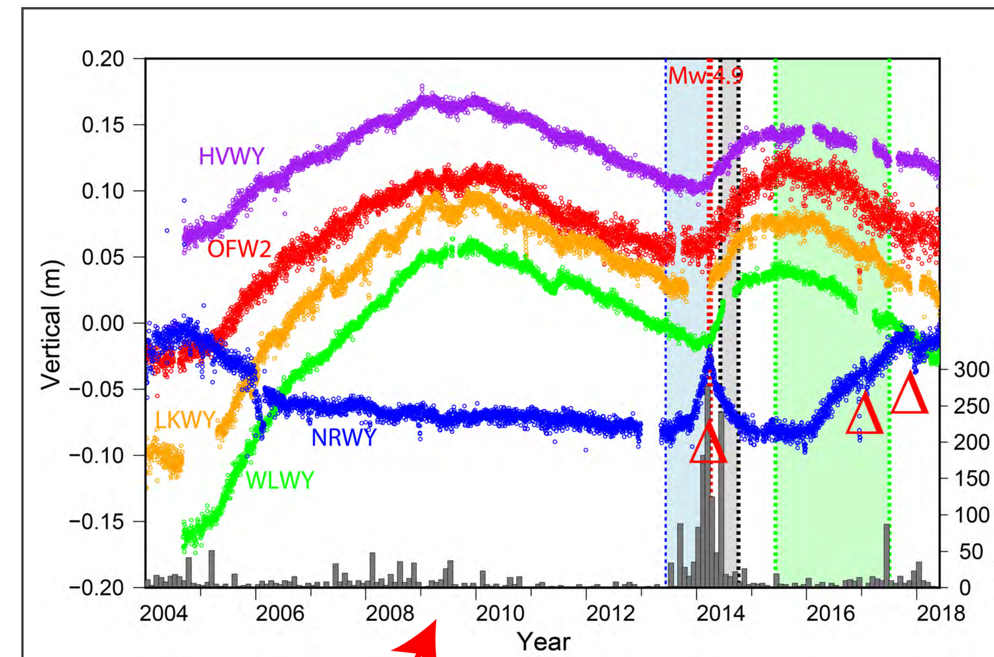

Figure 2 --Time series of vertical surface displacements (left axis, arbitrary zero) and monthly numbers of earthquakes (right axis, histogram at bottom) within the caldera and near Norris Geyser Basin from 20040101 to 20180601. Earthquakes are those that fall within the 15 km radius white circle in Figures 3b, c. The color-coded daily solutions are for the five labeled GPS stations in Figure 1. The time spanned by GPS measurements in Figure 3b is delimited by the blue rectangular area, the time spanned by the interferogram in Figure 3b is delimited by the gray rectangular area, and the time spanned by the interferogram in Figure 3c is delimited by the green rectangular area. Three red triangles below the time series for NRWY mark significant short-term reversals in uplift.

Figure 3 -- InSAR and GPS spanned time intervals are shown in Figure 2. (a) ERS2 interferogram showing uplift during 2000 episode. (b) TerraSAR-X interferogram showing subsidence during 2014 episode. GPS vectors show peak uplift. Yellow star shows epicenter of Mw 4.9 earthquake. Also shown is a Global Centroid-Moment-Tensor (CMT) solution for the earthquake (http://www.globalcmt.org). (c) Sentinel 1 interferogram showing uplift during 2016 episode.

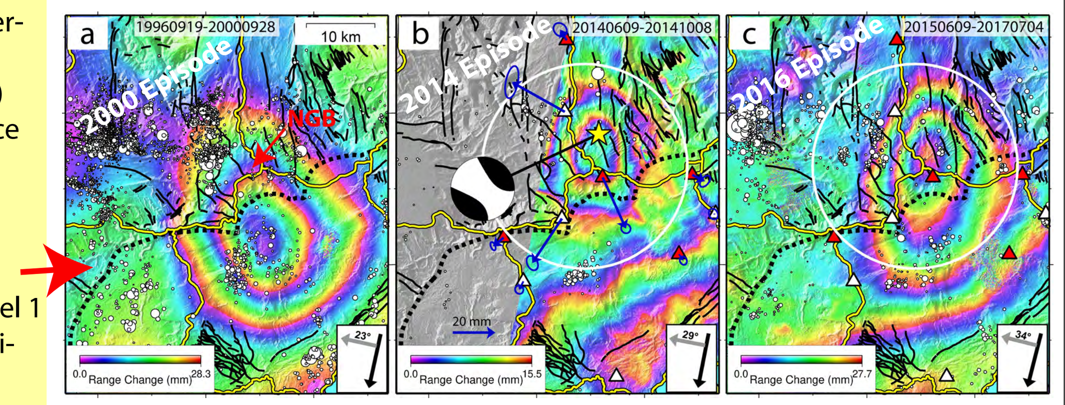

III. Model

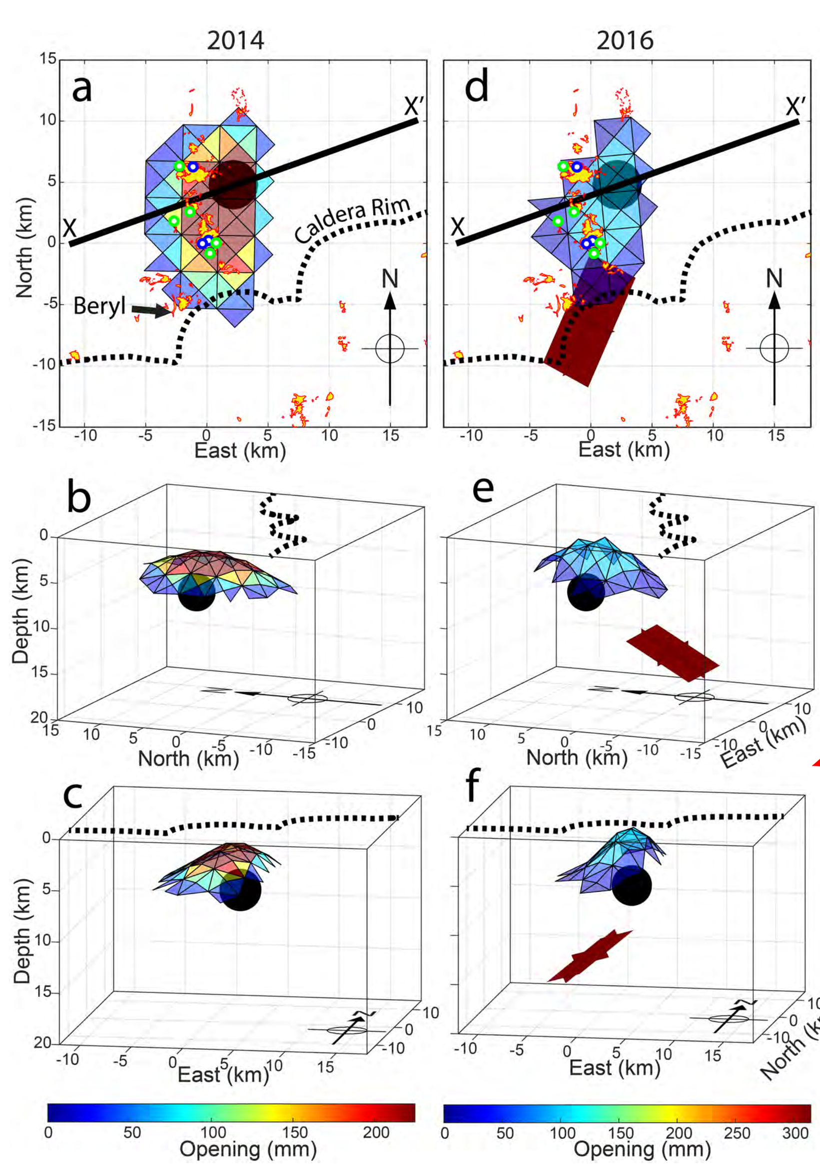

We used non-linear methods and Monte Carlo starting models to model all available GPS offset data (from continuous and semi-continuous stations) and InSAR data from five radar platforms to find our preferred deformation sources (Figures 4 and 5). The sources for the 2014 and 2016 episodes are domed distributions of triangular dislocations (Nikkhoo and Walter, 2015) described by two separate 2-D Weibull distributions (Myrhaug and Rue, 1997). The 2016 deformation also requires a deeper compensated dislocation source (Nikkhoo et al., 2017).

Figure 4 -- Deformation sources for the 2014 and 2016 episodes. The 4-km diameter black sphere shows the location of the Mw 4.9 earthquake (Figures 2, 3). The plan views in (a) and (d) show the mapped active thermal areas as yellow areas with a red outline, historic hydrothermal explosions are shown as green circles, and hydrothermal explosion craters greater than 100 m diameter are shown as blue circles (Christiansen et al. 2007). Line X-X' shows cross-section in Fig. 5.

Figure 5 -- Location map, and cross-section through NGB. **(a)** Epicenters (white filled circles) for the last 25 years of seismicity. The yellow-filled circle marks the location of the Mw 4.9 earthquake. **(b)** Cross-section through X-X' showing the 2014 source, blue lines; 2016 source, red lines; 2010 source, and green line. EQs within 4 km of X-X' are gray, within 2 km are yellow. The location of the Mw 4.9 earthquake is shown with the yellow star. Error bars to top of the sources are in the upper right.

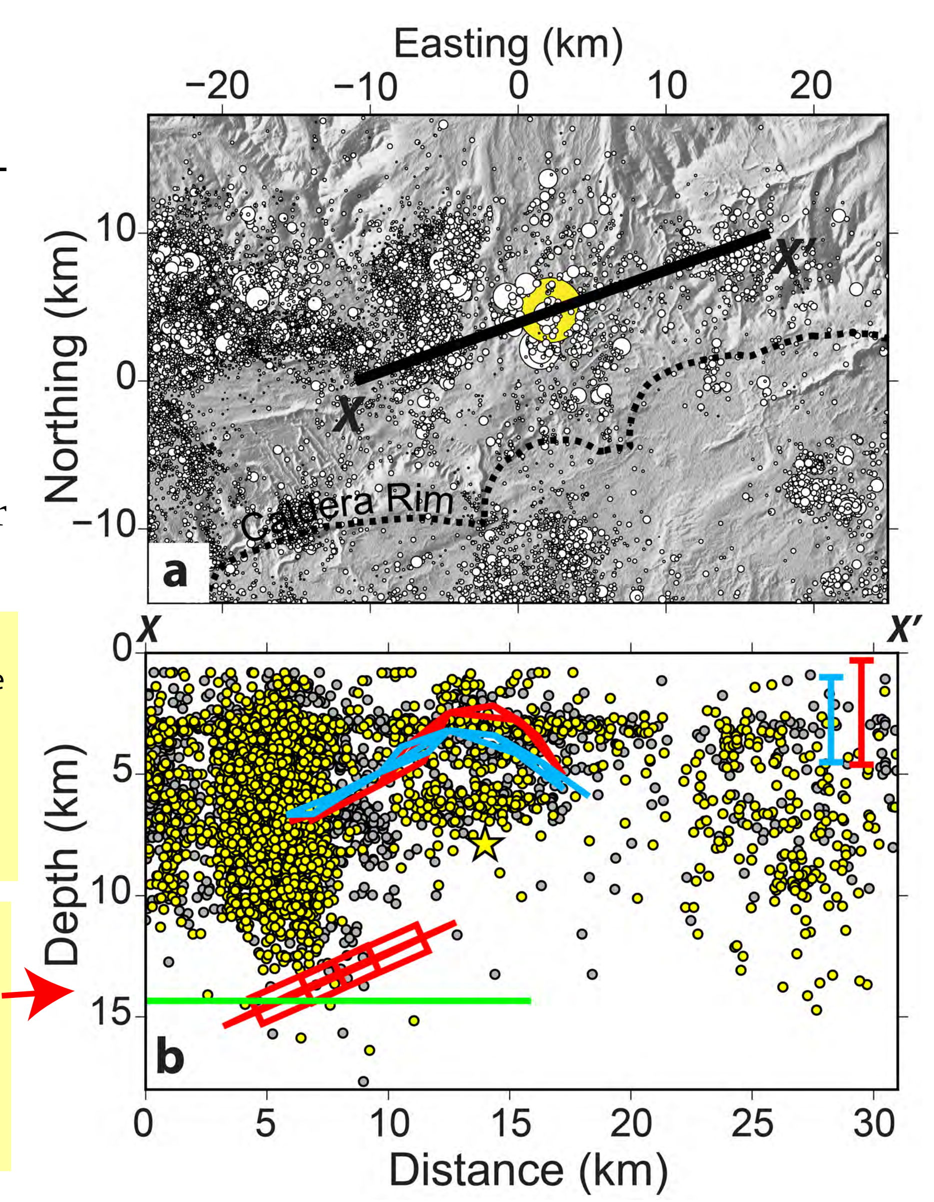

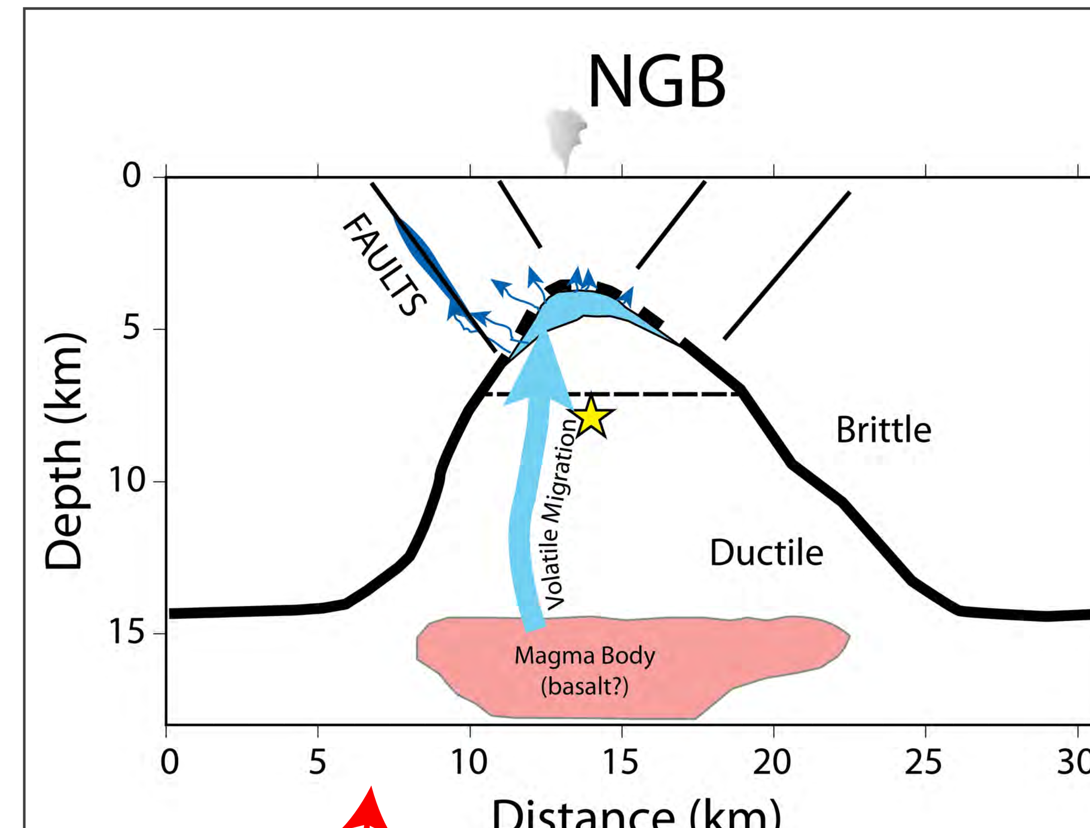

Figure 6 -- Schematic cross-section looking north along the axis of the Norris-Mammoth corridor, showing a model like that described by Fournier (1999) that is responsible for the deformation episodes near NGB. The yellow star shows the location of the 20140330 Mw 4.9 earthquake. The thin black lines depict the network of faults that correspond to the subsidence structure of the Norris-Mammoth corridor which extends north from the north caldera rim, through NGB, to just north of the Park boundary. The corridor is defined by active normal faults, high seismicity, active thermal features, and post-caldera eruptions.

IV. Conclusions

1. Modeling suggests accumulation of fluids at 2-3 km depth beneath Norris Geyser Basin (and possible shallowing with time, Figs. 4-6).

2. Accumulated fluids could be volatiles derived from magma emplacement ~14 km depth during 2000 episode.

3. The 20140330 Mw 4.9 earthquake might have occurred during a major breach of a permeability barrier, with possible minor breaches indicated by temporary reversals of uplift during the 2016 episode (Fig. 2).

4. Uplift at Norris Geyser Basin is likely related to a record number of eruptions of Steamboat Geyser and it could also indicate an increased risk of hydrothermal explosions in the Norris area.

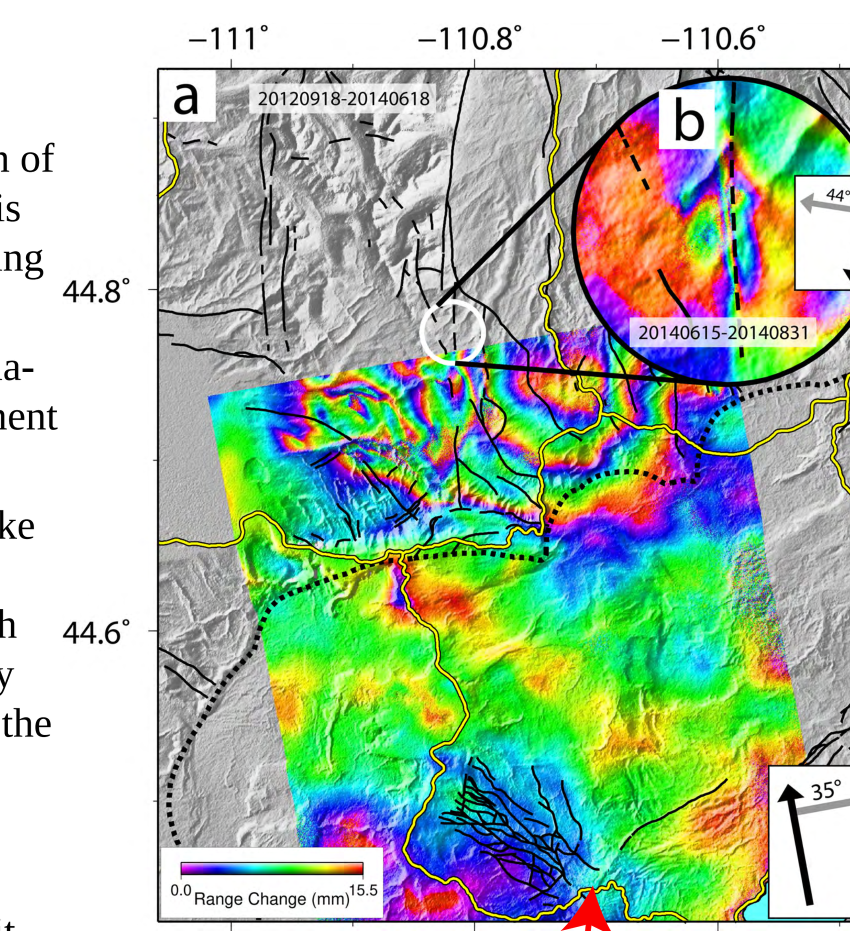

Figure 7 -- TerraSAR-X Interferograms showing small-scale deformation features that might result from volatiles escaping to the surface west of NGB after the 20140330 Mw 4.9 earthquake. (a) 20120918 to 20140618, (b) 20140615 to 20140831.

References

Christiansen, R. L., Lowenstern, J. B., Smith, R. B., Heasler, H., Morgan, L. A., Nathenson, M., Mastin, L. G., Muffler, L. J. P. & Robinson, J. E. (2007). Preliminary assessment of volcanic and hydrothermal hazards in Yellowstone National Park and vicinity. U. S. Geological Survey Open-file Report 2007-1071, 94p, https://pubs.usgs.gov/of/2007/1071.

Fournier, R. O. (1999). Hydrothermal processes related to movement of fluid from plastic into brittle rock in the magmatic-epithermal environment. Economic Geology, 94, 1193-1212, doi:10.2113/gsecongeo.94.8.1193.

Myrhaug, D., & Rue, H. (1998). Joint distribution of successive wave periods revisited. Journal of Ship Research, 42, 199–206.

Nikkhoo, M. & Walter, T. R. (2015). Triangular dislocation: an analytical, artefact-free solution. Geophysical Journal International, 201, 1119-1141. doi: 10.1093/gji/ggv035.

Nikkhoo, M., Walter, T. R., Lundgren, P. R. & Prats-Iraola, P. (2017). Compound dislocation models (CDMs) for volcano deformation analyses. Geophysical Journal International, 208, 877-894. doi: 10.1093/gji/ggw427.

Contacts

Charles Wicks (cwicks@usgs.gov) USGS, 350 North Akron Road, Moffet Field, California, USA 94035.

Dan Dzurisinn (dzurisin@usgs.gov) USGS, David A. Johnston Cascades Volcano Observatory, 1300 SE Cardinal Court, Vancouver, Washington 98683

Jacob Lowenstern (jlwnstrn@usgs.gov) USGS, David A Johston Cascades Volcano Observatory, 1300 SE Cardinal Court, Vancouver, Washington 98683

Jerry Svarc (jsvarc@usgs.gov) USGS, MS 977, 345 Middlefield Rd, Menlo Park, California 94025.

Acknowledgments

TerraSAR-X data were made available by the Deutsches Zentrum für Luft- und Raumfahrt (DLR) through DLR projects GEO1142 and GEO1742. ALOS-2/PALSAR data are copyright by the Japan Aerospace Exploration Agency (JAXA) and the Japanese Ministry of Economy, Trade and Industry (2015, 2016) and were made available through JAXA project P1216002. Radarsat-2 data were made available by the Canadian Space Agency through MDA Geospatial Services via the COMSAR initiative with the National Geospatial-Intelligence Agency.